FABRICATION AND APPLICATIONS OF PILLAR BOWTIE NANOANTENNA ARRAYS

BY

ABDUL MONNAF BHUIYA

THESIS

Submitted in partial fulfillment of the requirements
for the degree of Master of Science in Electrical and Computer Engineering
in the Graduate College of the
University of Illinois at Urbana-Champaign, 2015

Urbana, Illinois

Adviser:

Associate Professor Kimani C. Toussaint, Jr.

Abstract

This thesis reports the fabrication technique and applications of a pillar bowtie nanoantenna (p-BNA). We use different tools to fabricate our nanostructure, namely, electron lithographic tools, evaporator and plasma chambers. The theory of operation of the machines, especially electron beam lithography for higher resolution, electron beam evaporation for thin film deposition, reactive ion etching (RIE) for high aspect ratio pillar nanostructure and scanning electron microscopy (SEM) for imaging, has been presented. We carefully explain the reasons for choosing each parameter of each tool. For electron beam lithography, we look into the accelerating voltage and dosage parameters to get a high resolution nanostructure. Then we look into electron beam evaporation to come up with the thicknesses for metal deposition. Finally, we come up with the gas flow, pressure, power and etch time parameters for reactive ion etching (RIE) to complete the fabrication of the p-BNA structure. We demonstrate different experiments to show its usefulness in various areas of nanotechnology. We explain the theory to reduce the gap between pillar bowtie nanoantennas using SEM and experimentally show gap size controllability using a combination of accelerating voltage, current and magnification of SEM. Recording near field optical intensity in our nanostructure has been explained via simulation, fabrication and experimental results as well. Moreover, its use in the near infrared wavelength regime as a plasmonic sensor has been theoretically and experimentally demonstrated by increasing the size of the bowtie nanoantennas.

Finally, we propose some exciting future work for our p-BNA structure to show its versatile applications in the field of nanotechnology.

Acknowledgments

I wish to express my most sincere appreciation to my advisor, Professor Kimani C. Toussaint Jr. I learned the importance of diligence and integrity from him. He has helped me reach my accomplishments in the past years through immense support and guidance. I am especially grateful to Dr. Brian Roxworthy and Dr. Hao Chen for helping me through the experiments in the PROBE lab. They have been my mentors throughout the process and excellent colleagues to work with. I would also like to express my gratitude to the other members of the PROBE lab, namely Qing Ding, Mahfuzul Kabir, Woowon Lee, Dr. VVG Inavalli and Emeka Okoro, for sharing their knowledge and providing valuable support. Finally, I would like to thank my parents, my siblings and my friends for giving me the encouragement and strength to carry this work forward.

Table of Contents

Chapter 1

Introduction

1.1 Overview

In 1886, for the first time, an emission/collection metallic device later called an "antenna" was demonstrated by Heinrich Hertz [1] which allowed the reciprocal conversion of electromagnetic waves to electric currents in a conductor in the RF regime. That opened up a whole new area of research utilizing the antenna for various applications. But to operate them in the optical frequency regime, the antenna size has to be minimized because of the inverse relationship between length and frequency. The miniaturization of an antenna is called a nanoantenna. An optical nanoantenna differs from RF antennas in a couple of other different aspects as well. One is that due to the high losses at optical frequencies, the assumption of perfect electrical conductor is no longer valid, and the other one is that at a nanoscale these metal structures interact much differently with light. This has opened a new field of research named "plasmonics" [2]. One of the fields of plasmonics looks at localized surface plasmons, where small metallic nanoparticles interact with light to create coherent oscillation of electrons [3]. This creates an induced dipole as shown in figure 1.1 and thus creates a high electric field enhancement. The high electric field enhancement happens because of the negative dielectric constant of metal. After solving Maxwell's equations, we find the electric field equations [4] shown below:

$$Ein = \frac{3\varepsilon m}{\varepsilon + 2\varepsilon m} Eo$$

$$Eout = Eo + \frac{3n(n.p) - p}{4\pi\varepsilon o\varepsilon m r^3}$$

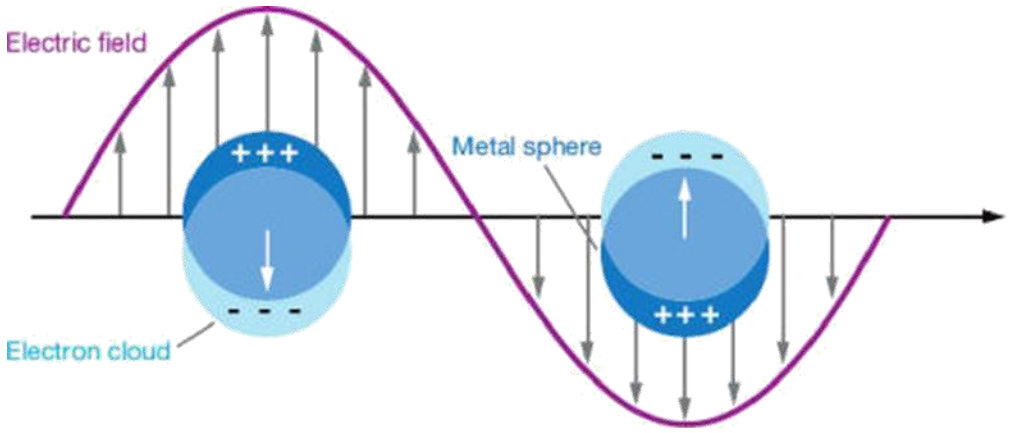

Figure 1.1: Electron charge density localization in metal nanospheres [5]

Here, E_{in} is electric field inside the metal sphere, ε_m the dielectric constant of the surrounding medium, ε the dielectric constant of metal, E_o the incident electric field and E_{out} the electric field outside the metal sphere. From the equation, we can see that if the dielectric constant of metal ε_m is equal to $-2\varepsilon_i$, then we get a huge enhancement in electric field. Also, if we put two or more nanoparticles together, they couple and, because of the hybridization model [6], increase the electric field enhancement. Because of the high field enhancement, these optical antennas which are a few hundred nanometers in size have several unique applications including single molecule sensing using SERS [7], plasmonic optical trapping [8], higher harmonic generation [9], optical imaging [10], energy harvesting [11] and various other applications. So, considering all these interesting effects, there has been a lot of effort put toward fabricating and characterizing the optical antenna.

The optical antenna offers several challenges, one of which is fabricating them with precise dimensions. Some of the main parts of fabricating a nanoantenna include lithography,

evaporation and etching, which all have their own challenges. This thesis addresses the details of all these main fabrication techniques and how we used these techniques to come up with the recipe to fabricate a pillar bowtie nanoantenna structure for various applications.

1.2 Organization of chapters

Chapter 2 presents the theoretical background on different fabrication techniques, mainly lithography, electron beam evaporation and reactive ion etching. Chapter 3 explains the recipe for fabricating the structure that we developed, called the pillar bowtie nanoantenna (p-BNA). It also includes the challenges and innovative ways that we used to fabricate the p-BNA structure. Chapter 4 presents the applications that we developed through the p-BNA structure. Chapter 5 covers the future applications and conclusion.

Chapter 2

Nanofabrication technique background

2.1 Lithography

The word lithography comes from two Greek words, ‘lithos’ and ‘graphein’, which mean ‘stone’ and ‘to write’ respectively. So, lithography means to write into something. There are different kind of lithographic techniques. The most used one is called photolithography and is mainly used for fabricating micron-scale structures [12]. A new emerging technique called electron beam lithography is now in use to fabricate nanometer scale structures. Both of them have almost the same principle to write except that the source for using photolithography is light and for electron beam lithography, it is electrons. Let us start with photolithography and as we go on we can address differences with electron beam lithography.

To understand the theory of photolithography, we have to understand the components that are essential to it. Figure 2.1 tabulates the components. One of the most important is photoresist, which makes it possible to write a desired pattern on a sample. It is a mandatory element for any kind of lithography.

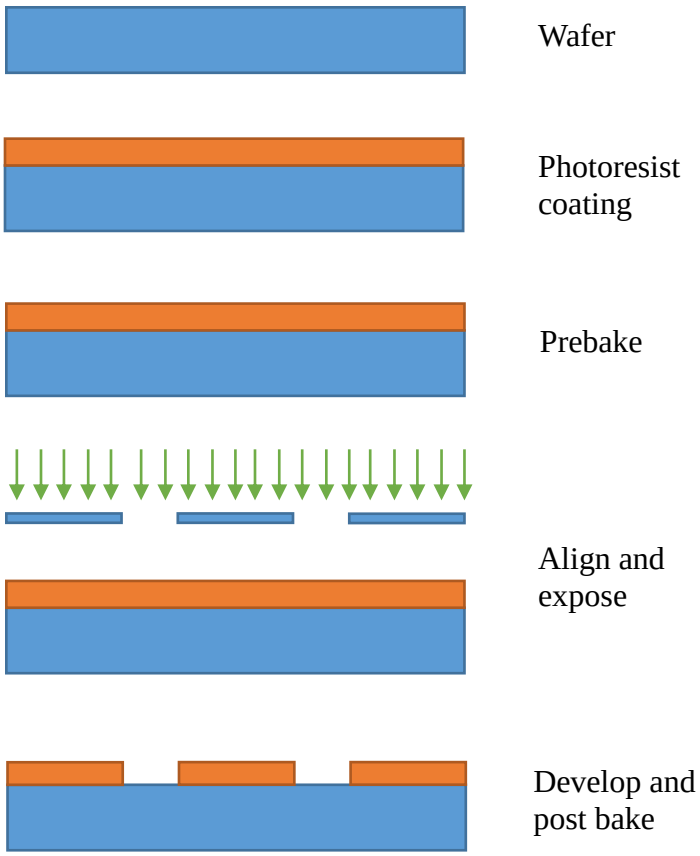

Figure 2.1: Full overview of a photolithography process

The principal components of photoresists are a polymer (base resin), a sensitizer and a casting solvent. When the source (electrons or light) is shined on the photoresist, the polymer changes its structure. To form a thin layer of the photoresist which is essential for higher resolution, a solvent is needed. The sensitizer controls the chemical reaction in the polymeric phase. There are mainly two different types of photoresist, the details of which are important to look into. One is called positive photoresist and the other one is called negative photoresist.

When the source is shined into positive photoresist, it weakens the polymer bonding between the main and side polymer chains by scission and thus, by experimental results shown in [12], the exposed resist becomes almost 10 times more soluble in the developing solution than in pre-exposure. After development, the photoresist looks like figure 2.2. Now, when the source is shined to negative photoresist, it strengthens the side polymer bonds by cross linking them with the main polymer bond and thus makes the exposed area insoluble in the developer solution. The process of negative photoresist is shown in figure 2.2 as well. The most common positive photoresist that has been used for both photolithography and electron beam lithography is PMMA (poly methylemethacrylate). On the other hand, the most used negative photoresist is SU-8.

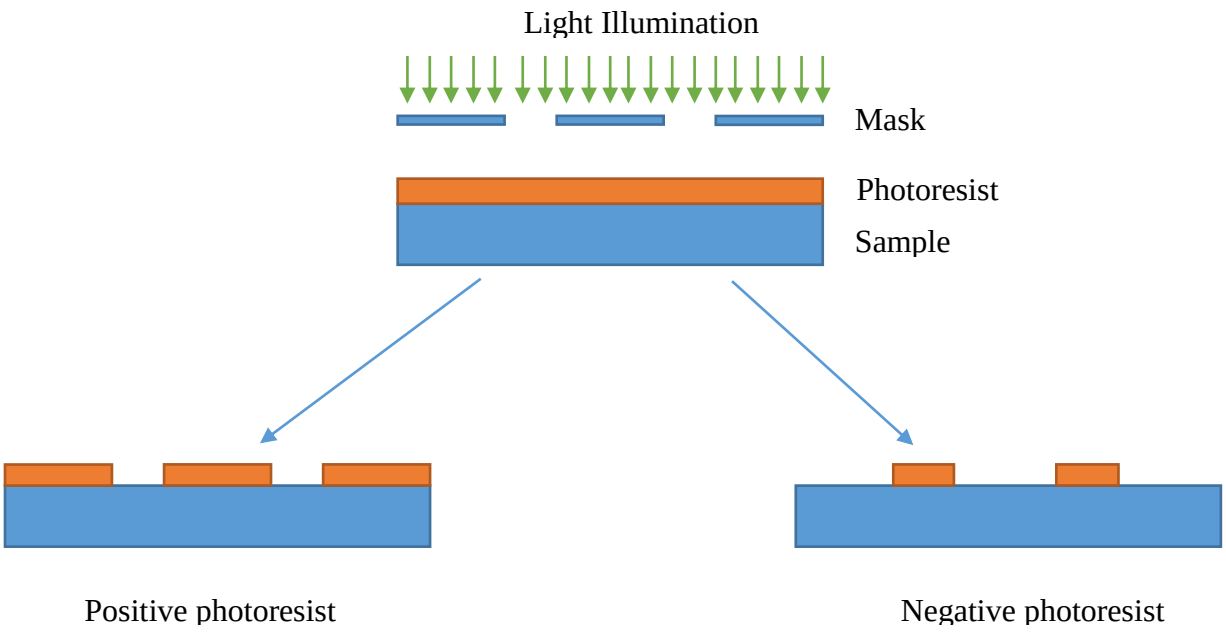

Figure 2.2: Positive and negative photoresist patterned substrate

Another fundamental aspect of lithography is the mask. The structure to make a desired pattern

on a resist coated substrate is called a mask. It is a nearly optically flat glass or quartz plate with an absorber pattern metal placed above the photoresist-coated surface, and the mask/wafer system is exposed to UV radiation. As shown in figure 2.2, the blue part of the mask absorbs the light where the white or transparent part of the mask let the light through and exposed the photoresist. There are also two kind of masks. They are called positive or dark field mask, which is a mask on which the pattern is clear with the background being black, and a negative or clear field mask, in which the pattern is dark with the background being clear. They are shown in figure 2.2 as well. But the thing to note here is that for electron beam lithography, the technique that has been used for fabricating the p-BNA structure does not need any mask. The way that electrons write a pattern is by the beam blanking technique, which essentially is to turn on the beam where you want to expose your photoresist and block the beam where you do not want to expose it. As the wavelength of the electron is much smaller, in this case, the resolution is going to be much higher. But this process is very slow because of the fact that going through each pattern one by one is going to take much longer than using a mask as a one shot exposure. So, we can understand the tradeoff for electron beam lithography, which is higher resolution in exchange for time. But as our p-BNA structure needs a gap between our bowtie nano-antennas to be around 20 nm, we chose electron beam lithography as conventional lithography cannot produce such a small gap size.

2.2 Etching

After the lithographic process is done, the next step can be one of two things. Either it can be etching using gas or chemicals, or it can be ion implantation or metal evaporation. In our p-BNA fabrication we have used metal evaporation first and then reactive ion etching (RIE). So, we are going to go over the theory of operation for those two methods in detail. We are going to start with etching in this part.

There can be two ways that we can etch a substrate. One is dry etching using different combinations of gases, and the other is wet etching using different combinations of acids. As stated earlier, we have used RIE and that is a part of dry etching, and thus we are going to talk about dry etching in detail with a bit of comparison with wet etching where it is necessary. In dry etching, the etched substrate which is a part of a sample is etched by gaseous species and compared with wet etching, it does not need any wet chemicals or rinsing and can leave the etching system in a dry state. Under the category of dry etching, there is a family of techniques that have been explained in [13] and can be used to increase the selectivity of etching or time of etching with respect to the other techniques. The techniques include the process of ion bombardment, chemical reaction through a reactive species at the surface, or combined physical and chemical mechanisms. One of the main components of dry etching involves the creation of plasma. Plasma is defined as ionized gas with equal number of ions and electrons. A more accurate definition of plasma is a quasineutral gas of charged and neutral particles exhibiting collective behavior [14]. Now, plasma-assisted dry etching can be categorized under two configurations, glow discharge etching (diode setup) or ion beam etching (triode setup) [13]. For the glow discharge technique, which is the technique that we have used for our p-BNA fabrication, plasma is generated in the same part of the vacuum chamber where the substrate is located, but for the ion beam technique, plasma is generated in a separate chamber from which ions are extracted and directed in a beam towards the substrate by a number of electrode grids. Our diode RIE setup consists of opposed parallel-plate electrodes in a chamber maintainable at low pressure, typically around 30-100 mtorr. The electrical potentials established in the reaction chamber, filled with gases such as CF_4 in our case, at a reduced pressure, determine the energy of ions and electrons striking the surfaces immersed in the discharge. After applying a voltage of around 1.5 kV between them, the electrodes separated by around 15 cm cause an electric field of 100 V/cm. Electrical breakdown of the CF_4 gas in the reactor will occur when electrons, accelerated in the existing field,

transfer an amount of kinetic energy greater than the ionization potential to the argon neutrals. That creates ions and free radicals of CF_4, which starts the etching mechanism which will be explained in chapter 3.

2.3 Electron beam evaporation

Electron beam evaporation is a technique which uses an electron beam controlled by a magnetic field to melt a metallic source to create thin film on a substrate [15] as shown in figure 2.3. It operates at a very low vacuum level to make sure that the mean free path of electrons is very high and at the same time to make sure that the thin film is not contaminated by any other particles around the chamber.

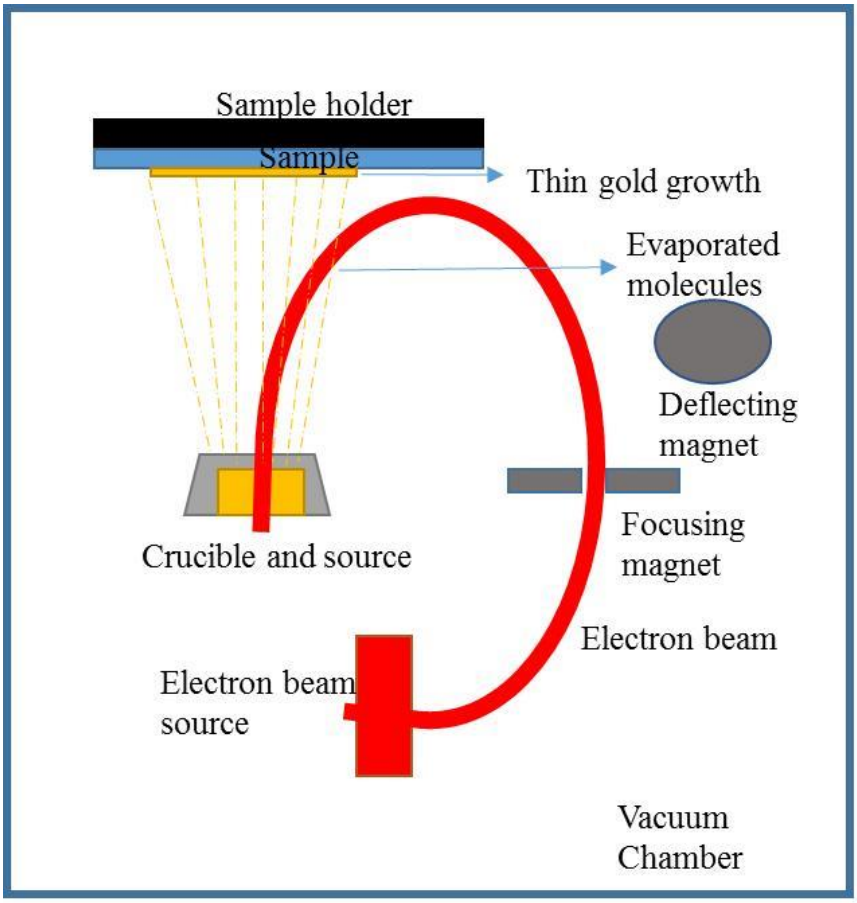

Figure 2.3: Electron beam evaporation overview

This is one of the reasons that we chose electron beam evaporation as well because if we have higher pressure like in plasma enhanced chemical vapor deposition (PECVD) or sputtering technique [15], we see that there is a possibility of contamination in there. Now we look at the thin film growth process for any deposition system, which involves three main steps. Firstly, it has to produce the appropriate number of atomic, molecular or ionic species. Then, through a medium, the molecules have to be transported to the substrate. Then, it has to condense on the substrate, either directly or via a chemical or electrochemical reaction, to form a solid deposition. The formation of this thin films into the substrate takes place via nucleation and growth processes. There are six steps by which we can explain the growth process. Firstly, the unit species that impact on the substrate lose their velocity component normal to the substrate and, because of their high kinetic energy gained at a low mean free path of the molecules at a lower pressure, they are physically adsorbed in the substrate. Then at that point, the adsorbed molecules are not in thermal equilibrium with the substrate and thus can move over the surface of the substrate, and because of that they interact among themselves and form bigger clusters. After the molecules are adsorbed, because of the thermal instability, the molecules can desorb with time which depends on the deposition parameter. Most of the time, this has been taken care of by making the chamber large enough so that the temperature difference between the source and the sample can be controlled. The adsorbed species start to grow in size if they interact with each other before getting desorbed. After reaching a critical size, the molecules become thermodynamically stable and the nucleation barrier is said to have been overcome. This step involving the formation of stable, chemisorbed, critical-sized nuclei is called the nucleation stage. Then after a saturation nucleation density is reached, the critical nuclei grow in number as well as in size. A parallel growth of nucleus to the substrate takes place by surface diffusion of the adsorbed species, and a growth perpendicular to the nucleus happens because of the direct impingement of the incident species. But the lateral growth at this stage is much higher than

the perpendicular growth. These grown nuclei are called islands. The next stage after forming the island is the coalescence stage. In that stage, the small islands start coating with each other in an attempt to reduce the substrate surface area. Because of the increased surface mobility of the adsorbed species, they form in a process termed agglomeration which happens because of increased temperature of the substrate. Now, at the final stage, larger islands grow together and the channels and holes of the uncovered substrate starts to get filled with the incremental metal deposition and thus create a continuous layer of thin film.

2.4 Scanning electron microscopy (SEM)

Going over the theory of operation of SEM in detail is important as one of our experiment was done by controlling the SEM accelerating voltage, current and magnification. The theory has been explained in detail in [16] but we will focus on the main components of SEM for our experiment as shown in the schematic of SEM [17] in figure 2.4. The components are the electron gun for accelerating voltage control, condenser lenses for current control and scan generator for magnification control. Starting with the electron gun which produces an electron beam for imaging, in our SEM (HITACHI 4800), we have thermoionic gun (TE gun) which emits electrons from a filament made of a thin tungsten wire by heating the filament at high temperature (about 2800k). By applying a positive voltage (1 to 30 kV) to the anode, these thermo-electrons are gathered as an electron beam.

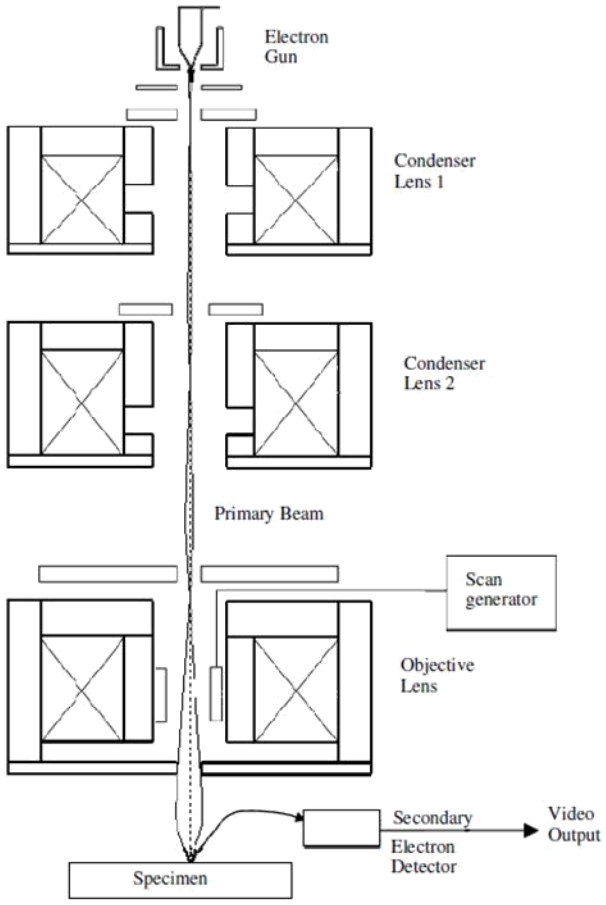

Figure 2.4: Full schematic of scanning electron microscope (SEM) [17]

Next are the condenser and objective lenses. These lenses are generally made out of magnetic lens. So, basically a lens action is produced when we pass a direct current through a coil wound electric wire and thus a rotationally symmetric magnetic field is formed. A strong magnetic lens can be formed when the density of the magnetic line is increased. So, basically placing a lens below the electron gun enables the adjustment of the diameter of the electron beam. By having the condenser lens and the objective lens in series, a small and fine electron beam probe is produced for a higher resolution image. To control the current follow, there is an "aperture" placed in between the objective lens and the condenser lens. The aperture controls how much of the beam goes to the objective lens

from the condenser lens. The number of electrons reaching the objective lens can be increased or decreased by increasing or decreasing the excitation of the condenser lens and thus making the electron beam broader or narrower respectively. So, it actually controls electron probe diameter and the probe current. After we control the probe current by condenser lens, we use an objective lens for focusing and this lens is responsible for the final diameter of the electron probe. So, it is very important to have a high quality objective lens to have an optimally fine electron probe. The current in the sample plane after it passes through the objective lens can be measured by fabricating a Faraday cup (shown in figure 2.5) in the sample holder and connecting it with a pico amp meter to measure the current.

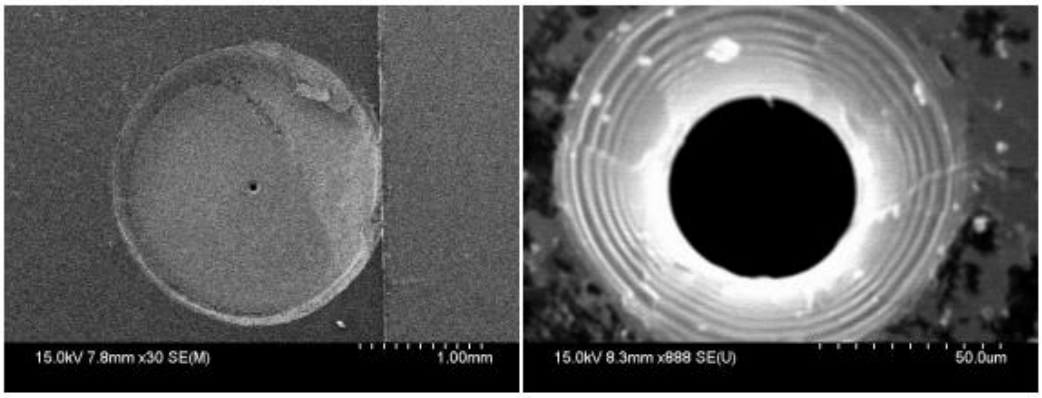

Figure 2.5: SEM after Faraday cup fabrication

Next, we will discuss the magnification of SEM. To see a SEM image on the monitor screen of the display unit, the specimen is scanned two dimensionally by the electron probe. So, by changing the scan width of the electron probe, we can change the magnification of the displayed SEM image. As we are not changing the monitor screen, decreasing the scan width increases the magnification, whereas increasing the scan width decreases the magnification. So, for example, if the size of the monitor is 10 cm and the scan width of the electron probe is 1 mm, the magnification is 100 times

and by changing the scan width to 10 um, the magnification changes to 10,000 times. So, magnification = D/d, where D is the display unit and d is the scan width of the electron probe. These are the important parameters that we used in our experiment described in section 4.1.

Chapter 3

Steps to Fabricate Pillar Bowtie Nanoantenna (p-BNA)

Having discussed the theory of operations that was needed to fabricate p-BNA, now we focus on the mechanism of building up a recipe to fabricate it. Figure 3.1 shows the schematic of the fabrication steps. Before going into details of each step to explain our recipe, we go through the process concisely as explained in [18]. First, we deposited 500 nm SiO_2 using plasma enhanced chemical vapor deposition technique. Then we performed our electron beam lithography patterning and came up with the bowtie nanoantenna pattern. Then we deposited 5 nm titanium as an adhesion layer of gold to SiO_2, 50 nm of gold to fabricate our plasmonic nanoantenna structure. As we were putting them on top of SiO_2 pillars, we performed RIE. But as gold physically sputters out of the nanoantenna during RIE, a hard mask of 8 nm nickel was used to protect the gold and then RIE was performed to fabricate the p-BNA structure. Now, we can go into detail of each step to understand the recipe for fabricating the p-BNA structure.

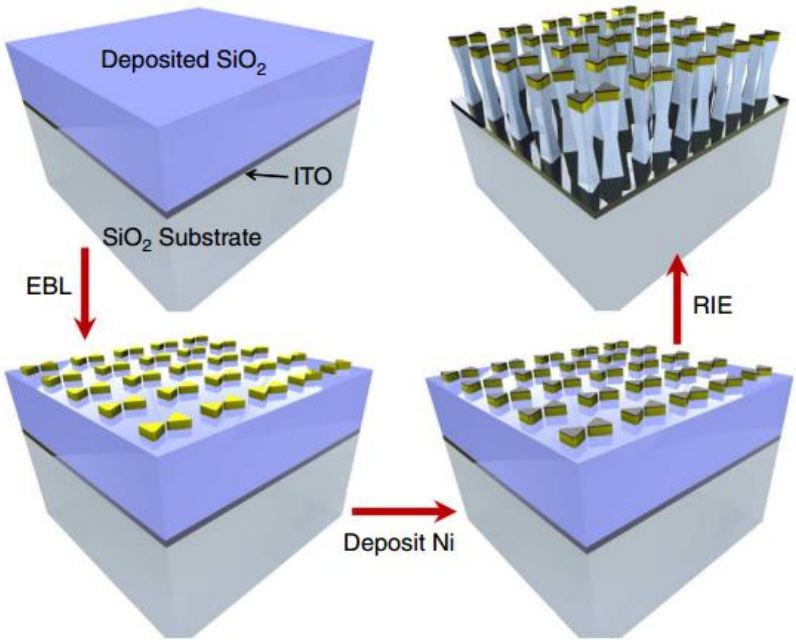

Figure 3.1: P-BNA fabrication steps. Begin with SiO_2 deposition, then electron beam lithography, then metal deposition and finally reactive ion etching to finish the fabrication [18].

3.1 Electron beam lithography

The first step to fabricate the p-BNA structure is to pattern it with electron beam lithography. We discussed above the choice of electron beam lithography, and there are several other issues to take into account to fabricate p-BNAs using electron beam lithography. One of the main elements to choose is the accelerating voltage. We can relate the De Broglie equation and the kinetic energy equations to come up with a relation between wavelength and accelerating voltage [19]

$$\lambda = h/mv$$

where is the wavelength of electron, *h* is Planck's constant, *m* is the mass of the electron and *v* is

the velocity of electron.

$$E = eV = \frac{mv^2}{2}$$

where *E* is energy, *e* is electron charge and *V* is the accelerating voltage. Combining the first two equations, we get

$$\lambda = \frac{h}{(2meV)^{1/2}}$$

Looking at the last equation, we can conclude that the higher the voltage, the lower the electron wavelength and thus the higher the resolution. So, firstly we chose the accelerating voltage to be 25 keV. The next important thing to consider in electron beam lithography is dosage, which can be defined by sensitivity of photoresist. Sensitivity is defined as the minimum electrical charge per unit area of resist film required for complete development of the exposed area and measured in coulombs per centimeter square. So, we can write dosage as the intensity of the electron beam source times the dwell time. For positive photoresist PMMA which has been used in our case, we can relate the PMMA fragment sizes and the exposure dose by the fragment size of PMMA. So, as the dose increases, the average fragment size of PMMA decreases and solubility in the developer increases. To come up with the optimal gap size between the bowtie nanoantennas, we have done a dose test by changing the dwell time of the electron beam on the photoresist. In figure 3.2, we can see the dose map going from 300 $\mu C/cm^2$ to 500 $\mu C/m^2$ and how the dose affects the gap sizes between the two nanoantennas after metal deposition. With the dose of 300 $\mu C/cm^2$, we get the dwell time to be lower and thus the gap between the nanoantennas to be higher, and with increasing dosage up to 500 $\mu C/cm^2$, we can see that the exposure gets too high and thus the two bowties get attached. We have to be careful in this case not to overexpose so that all the bowties are exposed and thus get washed away during development, or to

underexpose so that no bowties get exposed and the surface is entirely metal.

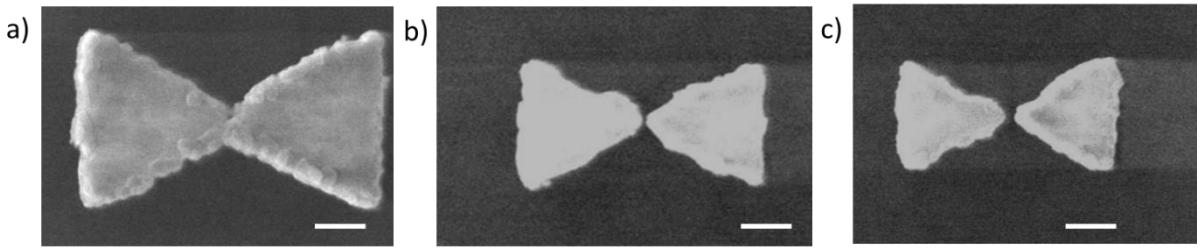

Figure 3.2: a) 500 μC/cm^2 dose, b) 400 μC/cm^2 dose, c) 300 μC/cm^2 for bowtie nanoantenna, 100 nm scale bar for a and 150 nm scale for b and c

Three bright field images are shown in figure 3.3 which show the underexposure, normal exposure and overexposure cases.

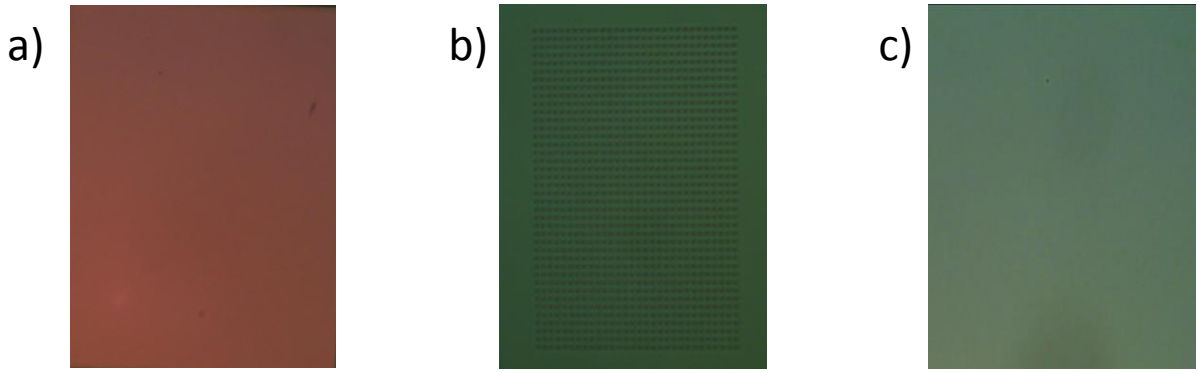

Figure 3.3: a) underexposed Bowtie nanoantenna array, b) optimal exposure of bowtie nano antenna array, c) overexposed Bowtie nanoantenna array

Once we have finalized our main points, accelerating voltage and dosage, there are several other issues that can help increase the resolution, but it is beyond our scope to discuss all the points in this thesis. Full detail can be found in [20]. We go over the steps for the full lithographic process that we used to give a broad idea of all the steps.

First of all, we clean our glass slide in piranha (3:1 ammonium hydroxide (NH_4OH): hydrogen per oxide (H_2O_2)) solution to remove any kind of organics or dust from it. Then we bake it in a hot plate at 200^{o}C for 15 minutes to dry it. Then we put it in the spinner, drop 100 mL of PMMA in it and spin it at 2000 rpm for 45 seconds. Then we soft bake it at 110^{o}C for 30 seconds. After that, with appropriate dosage and accelerating voltage, we expose the sample with desired pattern generated by the e beam machine. A sample pattern that has been developed by me in AutoCAD to convert to GDS for our structure is shown in figure 3.4.

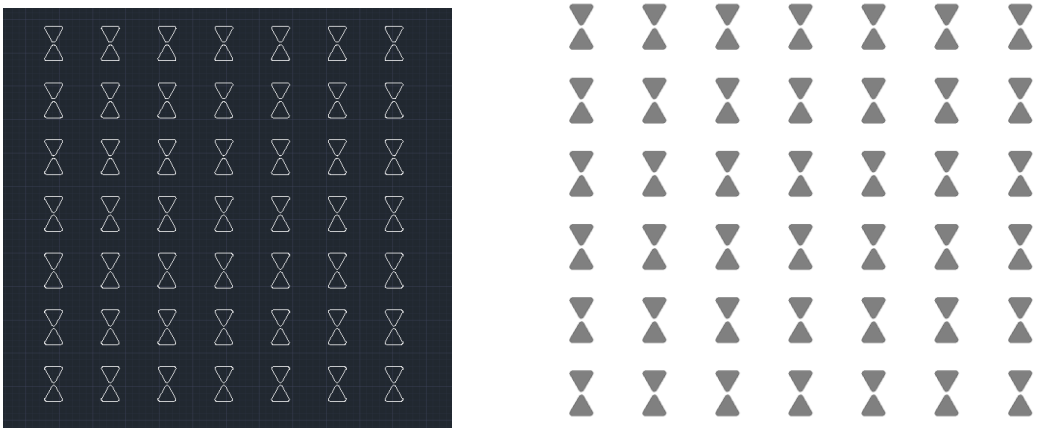

Figure 3.4: a) AutoCAD, b) GDS file for bowtie nanoantenna array

After exposure, the pattern was developed in MIBK:IPA 1:3 solution for 45 seconds at room temperature and inspected under a microscope to check for proper development and exposure. Then the patterns are ready for metal evaporation.

3.2 Electron beam evaporation

As discussed before, electron beam evaporation is the most common tool to evaporate any metals on a patterned substrate. In our case, we make gold bowtie nanoantennas, and as gold does not adhere

well to glass [21], we deposit 5 nm titanium prior to 50 nm gold deposition. After fabricating bowtie nanoantenna, we use reactive ion etching, which will be discussed in the next session, to fabricate pillar bowtie nanoantenna. In this case, we use nickel as a protective layer as the sputtering rate for gold during a collision with ions is much higher than that for nickel [22]. So, after we deposit titanium and gold, we deposit 8 nm of nickel so that it does not let gold sputter out of the bowtie nanoantenna. After depositing titanium, gold and nickel in the resist coated substrate, we put the sample in an acetone bath for 45 minutes to liftoff the resist and the excess metal. After liftoff we clean it with IPA (isopropyl alcohol) and blow dry it with nitrogen to have the bowtie nanoantenna sample ready. Zoomed out and zoomed in scanning electron microscope (SEM) images of the bowtie nanoantenna array are shown in figure 3.5

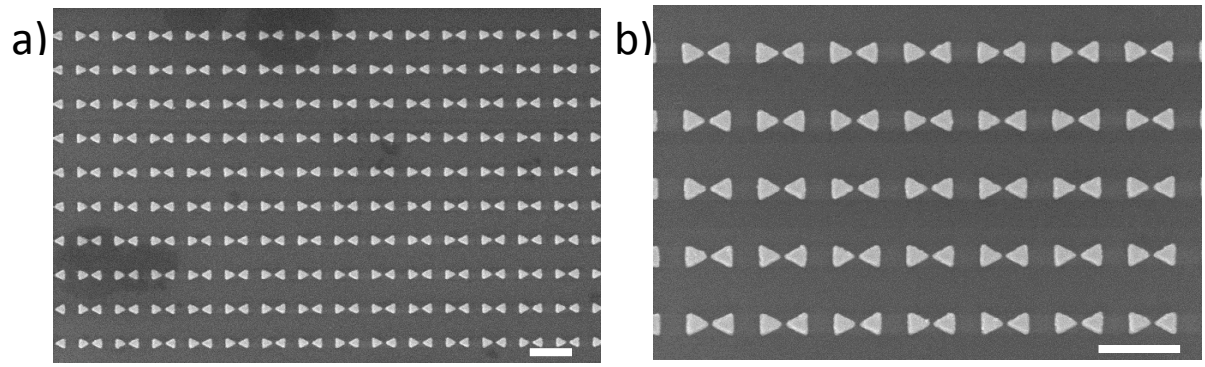

Figure 3.5: a) Zoomed out SEM of Ti/Au/Ni bowtie nanoantenna, b) Zoomed in SEM of Ti/Au/Ni bowtie nanoantenna, scale bar 400 nm

3.3 Reactive ion etching (RIE)

After metal deposition, to fabricate p-BNA, we have chosen to etch SiO_2 using reactive ion etching (RIE). As discussed before in the theory of operation for RIE, there are also several parameters to adjust to come up with the optimal pillar height with an ideal undercut of the pillars. The four parameters that we optimized to come up with the p-BNA recipe are pressure, gas flow, power and time. We are going to go through all of them to verify the reasons for choosing specific values for each of them.

First, we have chosen gas flow to be 35 mtorr because at high pressure, more molecules are available for the electrons to collide and thus generate plasma, i.e. ions, electrons and free radicals, which accelerates the etch rate by reacting with the substrate material. But at the same time increasing pressure too much will decrease the mean free path of the electrons and thus it will have less kinetic energy; therefore, it will be very difficult to generate the ions or free radicals, and thus plasma which will decrease the etch rate. That is why we chose 35 mtorr to have a balanced etch rate.

Next, we chose gas flow of CF_4 to be 70 sccm because CF4 is an electronegative gas and after colliding with electrons, it makes free radicals of fluorine ions (F^-) and CF_3^+ ions that can be very reactive to the substrate. Also, 70 sccm is experimentally chosen as more than 70 sccm flow rate will increase the atoms and thus decrease the electron mean free path, which will in the end decrease the plasma and thus reduce the etch rate. Also, at less than 70 sccm, the gas molecules will be lower to create highly reactive F- and CF_3+ to enhance the etching process. So, at 70 sccm, these radicals and ions create both physical and chemical etching. As the ions are accelerated towards the anode of the chamber where the substrate is sitting, they hit the substrate with high energy and create physical

etching. As mentioned before, this is why we have put down nickel so that it can protect gold as the physical sputtering rate for gold is much higher than for nickel. The reaction mechanisms for chemical etching are shown below to etch SiO_2 using CF_4:

(1) Formation of fluoric-radicals by impact ionization: $e^- + CF_4 \rightarrow CF_3^o + F^o + e^-$

(2) Formation of volatile silicon compounds: $SiO_2 + 4F^o \rightarrow SiF_4 (gas) + O_2$

(3) Dissociative ionization with attachment: $CF_4 + e^- \rightarrow CF_3^+ + F^- + e.$

In this case, the primary ions are: CF_3^+ and F^- . Neutral radicals are produced in smaller quantities and are CF_3^o and F^o. Assuming the substrate is biased, then CF_3^+ ions are accelerated toward the sample and F^- ions are generally repelled. On horizontal surfaces, however, ionic bombardment provides enough energy to cause the carbon to combine with surface oxygen. Released CO exposes the surface silica, which is removed by combining with released fluorine radicals. The uncharged F^o radicals will diffuse toward the surface and are the primary etch species. After that, the adsorption of F^o happens in the substrate and F^o first reacts with exposed dangling bonds at the surface, then more radicals start breaking the substrate bonds and create SiF_4 volatile gas. After that, SiF_4 gas desorbs which is assisted by ion bombardment of CF_3^+ ions. Volatile products diffuse away from the chamber via vacuum pump and the etching process completes. This whole process is shown in figure 3.6.

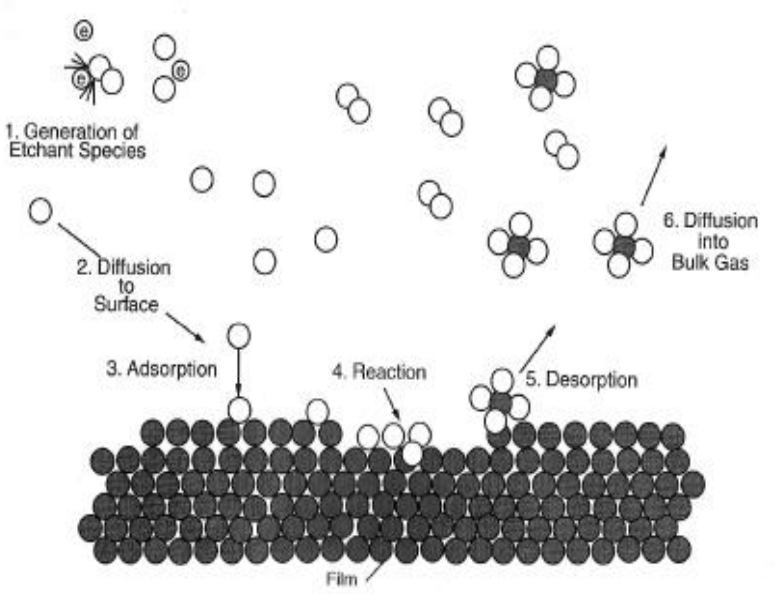

Figure 3.6: Reactive ion etching process overview [12]

We can also add O_2 in this process to enhance the etching rate because it is less electronegative and thus bonds with C atoms to form CO or CO_2 so that the carbon is not going to bond with F radicals or ions. But O_2 also increases the undercut of the pillars because of higher chemical etching than physical etching, and thus we chose not to add it with CF_4 as we had ~15 nm undercut already by just adding CF_4.

Another important parameter is the power of the RIE machine. On one hand, increasing the power increases the density and energy of the free electrons, which in turn increases the etch rate. On the other hand, increasing the power also increases the physical etch rate in addition to the chemical etch rate and thus will sputter out metals as well. So, we set our power at 90 W.

Then we experimentally examined the etch rate with the above mentioned parameters with a profilometer. We see that the etch rate for our PlasmaLab Freon RIE machine for the p-BNA is around 25 nm / minute. So, we etch our structure for around 20 minutes to come up with ~500 nm SiO_2 pillar bowtie nanoantenna structure. In figure 3.7, we show the 25° and 75° SEM images of the gold nanoantenna pillars on top of 500 nm SiO_2 pillars after etching for 20 minutes.

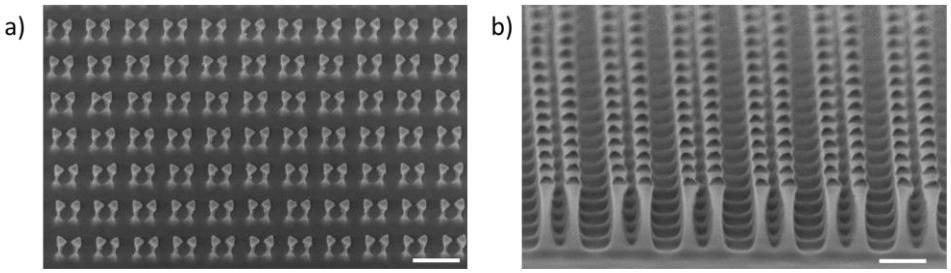

Figure 3.7: a) Normal and b) 75° SEM image of the P-BNA after reactive ion etching. Scale Bars, 400 nm.

Chapter 4

Application of Pillar Bowtie Nanoantenna (p-BNA)

4.1 Reduced gap nanoantenna

4.1.1 Experimental results for p-BNA

One of the interesting applications of the p-BNA is to use the mechanical degree of freedom of this kind of elevated structure to tune the gap between the structures. We use the p-BNA structure to couple the intrinsic mechanical and electromagnetic degree of freedom via gradient forces to tune its gap to a desired value. Using a standard SEM, individual nanoantenna gap sizes can be controllably tuned down to 5 nm, about one quarter of what can be achieved by conventional electron beam lithography.

By using a standard SEM (Hitachi 4800), we caused the gap of the nanoantennas to be reduced by the gradient force of the electron beam [23]. The whole process has been captured in figure 4.1 where in figure 4.1a, the top view of the p-BNA is shown and in figure 4.1b, the 45^{o} tilted view is shown and both of them show the gap sizes between the antennas to be around 30 nm. Then we have controlled the accelerating voltage, current and magnification of the SEM machine to control the gap sizes between them, which is going to be discussed after this part. So, again figure 4.1c and 4.1d show the top view and the 45^{o} tilted view of the p-BNA respectively and by using 10 keV, 180 pA current and 800k magnification, we can reduce the gap size down to 20 nm in about 10 seconds and we can zoom out to make them stay at that gap size. Again, by using 10 keV, 180 pA current and 800k magnification, we can reduce the gap size down to 5 nm in about 20 seconds, which is shown in figure 4.1e and 4.1f, and zooming out again will let them stay with that value of the gap. This fact

can be explained by plastic deformation via the electron beam, which makes the nanoantennas stay in their respective positions. There have been previous reports on this kind of behavior in the literature, for example, Zheng et al. [24] describe a "bond-switching" mechanism, whereby broken or dangling bonds between oxygen and silicon atoms in amorphous silica particles and nanowire structures can reform the nearby atoms, which gives rise to migration of defects through the structure. This process can also be viewed as a healing mechanism that prevents excessive formation of the voids in the SiO_2 and this mitigates the crack formation and increases ductility. Theoretical studies have also been performed to show the plasmon mode that gets excited in metal nanoparticles due to the interaction with a beam of fast moving electrons via an attractive gradient force towards the beam.

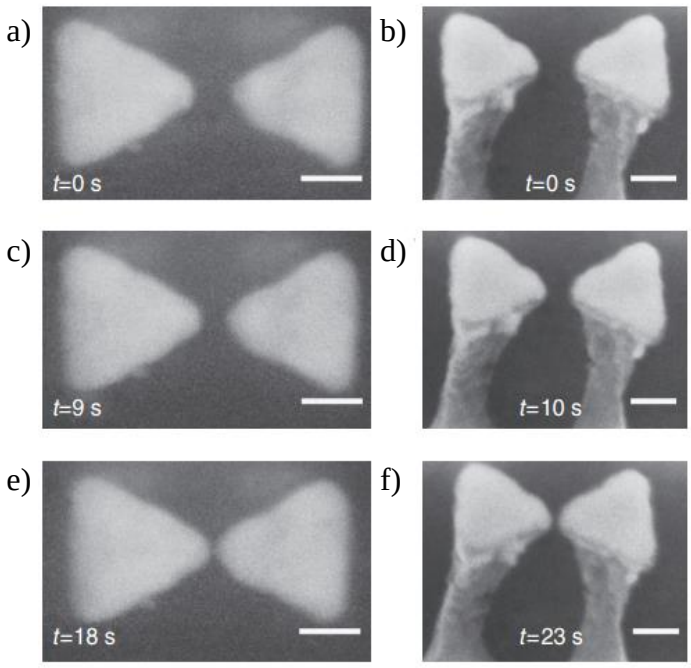

Figure 4.1: a-b) Normal and 25° SEM image of the P-BNA before e-beam incident, c-d) normal and 25° SEM image of the P-BNA after ~10 seconds of e beam irradiation, e-f) normal and 25° SEM image of the P-BNA after ~20 seconds of e beam irradiation [20]. Scale Bars, 50 nm.

To understand the controllability of the gap size between the two nanoantennas, we have gone through different voltages and magnifications in a specific current value to come up with the desired curves shown in figure 9a and 9b. The techniques to control the current and voltage have been explained in the theory section about SEM. So, we have chosen an accelerating voltage (Vacc) and magnification (M) using real-time video capture of the SEM display. In figure 4.2a, we made the magnification of the SEM to be constant at 800k, current to be constant at 180 pA and used increasing voltages to come up with a desired recipe for time, and with that we can reduce the gap to a desired value. For example, if we look at the black curve which shows the accelerating voltage to be 20 keV and see the gap sizes, we can see that we can go from 30 nm to about 15 nm in around 4 seconds and in the case of 15 keV (red curve), we can get the same gap size but with more time, around 7 seconds. If we want to look at them in terms of velocities, the velocities are around 2.1 and 2.8 $nmsec^{-1}$. The reason for that is as we increase the voltage, that increases the power of the beam as Power = Current*Voltage; thus a higher power beam reduces the gap sizes much faster. Also, we can do almost the same experiment but this time keeping the accelerating voltage and the current to be constant at 20 keV and 180 pA respectively and change the magnification of the SEM from 450k to 800k. So, in this case, increasing magnification shrinks the area scanned by the electron beam, thereby increasing the number of electrons interacting with the p-BNA, which in turn increases induced electromagnetic forces; thus, we can see in figure 4.2b that increasing the magnification reduces the time it takes to reduce the gap size between the nanoantennas.

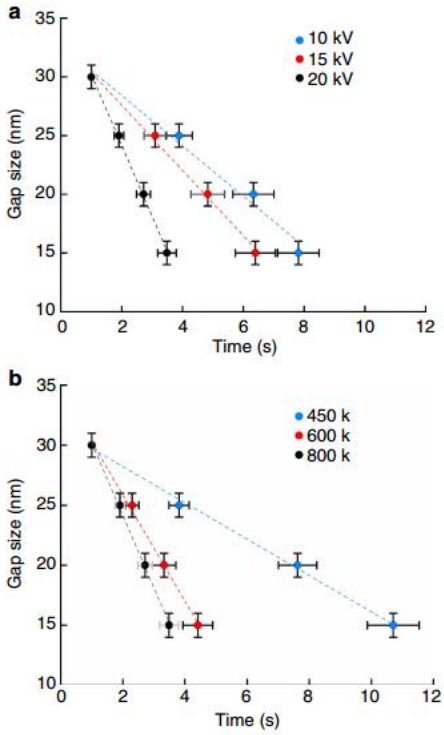

Figure 4.2: P-BNA deformation: a) Vacc changed with fixed Magnification at 800k, b) Magnification changed with fixed Vacc = 20 KV [20]

4.1.2 Theory of electron beam induced gradient force

We have seen experimentally that electron beam induced gradient force from SEM can fabricate a reduced gap plasmonic pillar structure, but to understand it fully, I am going to present the theory of the gradient force by electron beam. This process is heavily dependent upon the position of the beam with respect to the particle in the x and y directions shown in figure 4.3a and 4.3b, and it results from the fast moving electrons to create an attractive force towards the beam [25-28]. For certain x and y coordinates, the nanoantennas, due to repulsive gradient force, repel each other, and that plasmonic mode is called the ‘dark’ plasmonic mode [26]. However, as we see in figure 4.3b, at most of the other position there is a net attractive gradient force.

The origin of the net attractive force can be explained by looking into the 'ingap' plasmonic modes over 'outside' plasmonic modes and the evanescent field of passing along the z axis, which is given by [29]

$$E = \frac{2Newq}{ve^{2\Upsilon\varepsilon o}}\left[-\frac{K1\left(\frac{wr}{ve\Upsilon}\right)\boldsymbol{r}}{r} + \frac{i}{\Upsilon}Ko\left(\frac{wr}{ve\Upsilon}\right)z\right]e\left(\frac{iw}{vez}\right)$$

Here Kj is a modified Bessel function with order j, e is the electron charge, ve is the electron velocity, εo is the free-space permittivity, I is the imaginary unit, $y = 1/sqrt(1-(ve-c)^2)$ is the Lorentz contraction factor, r = (x-xo,y-yo) r =|r|, z is the unit vector along the z direction and Ne is the number of incident electrons passing through the scanned area (Ascan) per second given by $Ne=Ie(\pi wo^2)^{-1}$. Here, w_o = 1 nm is the beam radius produced by the SEM, Ie is the beam current at the sample and w is the frequency of the electron beam which can be considered as spanning a broad supercontinuum [25]. Again as we see in figure 4.3a and 4.3b, symmetric passage of the beam through the gap enhances electric field intensity on the outside edges of the structure and tends to pull the p-BNAs apart [26,28], but the large in-gap intensities produced in the asymmetric cases induce significant gradient forces on the gold nanoantennas towards the gap center. If we look at figure 4.3b, we can see that there are many more in-gap modes and thus the overall gradient force is attractive. The forces are in the range of nN, an order of magnitude larger than previously reported values and these values are also consistent with our theoretical force magnitudes to achieve the experimentally observed p-BNA deformation.

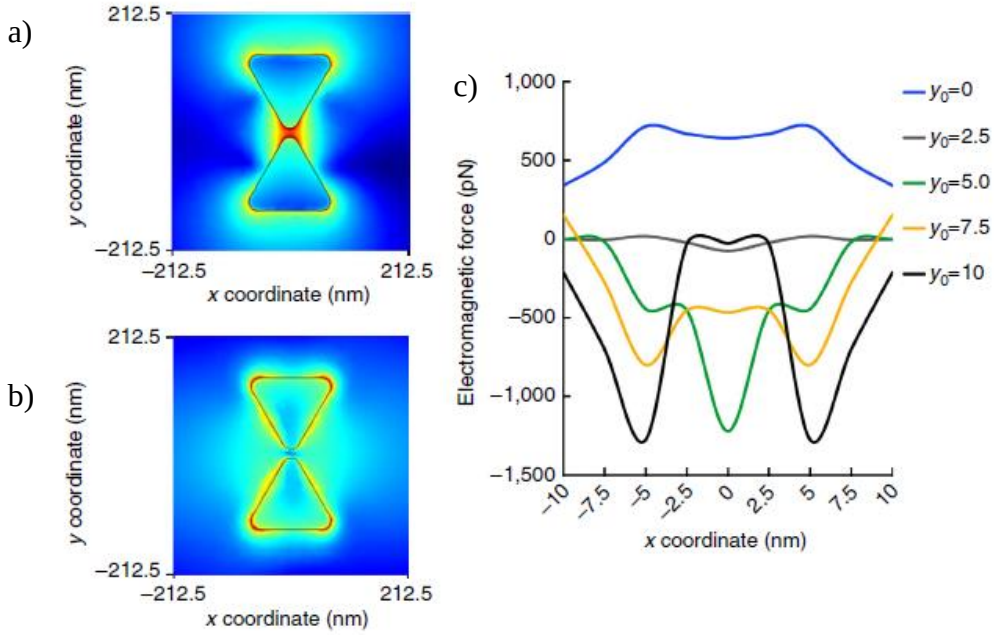

Figure 4.3: Normalized electric fields for a) an in-gap mode due to illumination with impact parameters (x0, y0) = (0,5) nm, b) an outside mode due to symmetric illumination with impact parameters (x0, y0) = (0,0) nm, and c) electromagnectic force acting on the upper antenna arm for electron beam impact [20]

4.1.3 Experimental results for SiO_2 pillar structure

We also have done comparison between gold p-BNA for excitation of plasmonic mode and without gold, only the SiO_2 pillar structure, to verify that the proposed mechanism of electron beam induced gradient force is indeed responsible for the observed p-BNA deformation. So, the SiO_2 pillar structure has been fabricated by etching metals from the top of the pillars. The first step to etch Ni and organic contaminants was to put the sample in piranha solution (3:1 sulphuric acid (H_2SO_4): Hydrogen peroxide (H_2O_2) for 30 seconds. Then the sample was submerged in deionized water and afterwards placed in a solution of 3:1:2 nitric acid (HNO_3), hydrochloric acid (HCl) and water for 30 seconds to the gold and the titanium adhesion layer. Then the sample was washed with deionized water and dried under a stream of high purity nitrogen. This process removes all the metals,

leaving the SiO_2 pillars unaffected. SEM images of just the SiO_2 pillars are shown in figure 4.4a and 4.4b.

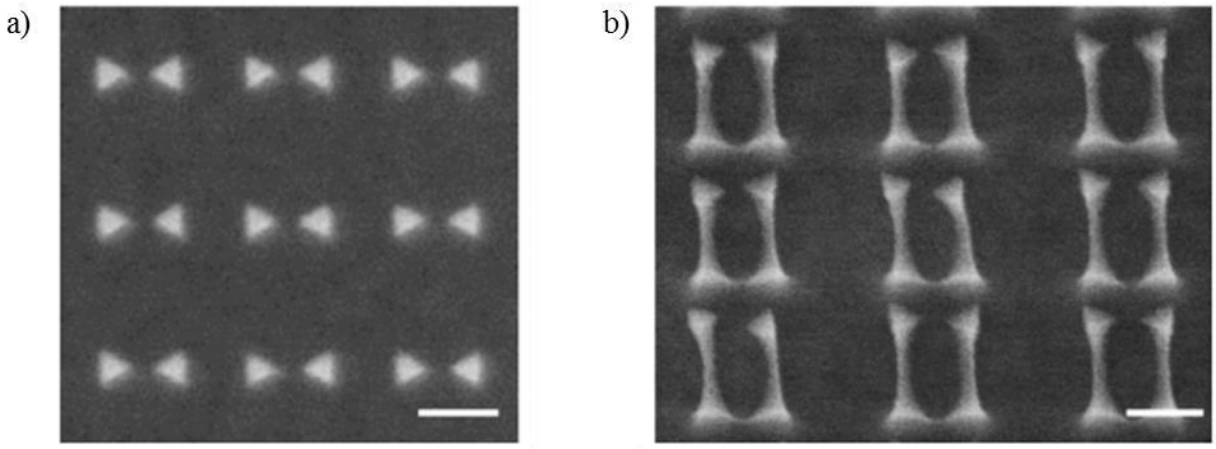

Figure 4.4: a) Top and b) 30^0 view of P-BNA without metals [20]. Scale bars, 250 nm

These SiO_2 pillars are exposed to electrons with an accelerating voltage, magnification and beam current of 20 keV, 800 k and 180 pA respectively, and no deformation was seen on those nonplasmonic pillars. So, the observation suggests that plasmonic enhancement of the gradient forces induced on the structure plays a significant role in the p-BNA deformation. But as we have increased the current to be around 360 pA, which is double the current to have double the electron flow, via the evanescent field coupling on dielectric objects, the pillars started to attract each other [23]. The description of current measurement in the sample has been explained in the theory section of SEM.

The results of this work show a new way to reduce the gap between pillar bowtie nanoantennas by the electromagnetic degree of freedom which enables the reconfigurability of the p-BNAs, a process that is not possible using conventional existing techniques. This technique will benefit the future

plasmonic applications by, for example, enabling homogenization of nanoantenna gap sizes in an array, leading to sharper plasmonic resonances, or it can be used to engineer novel photonic devices whereby a single BNA or an array of nanoantennas is modified to yield different plasmonic responses in a very unique manner. This effect also has several advantages over conventional lithographic techniques, for example, reducing the cost by not using any photoresist and also reducing the proximity effect [30] that makes the fabrication of sub-20-nm nanoantennas difficult. Thus, along with offering very unique advantages over conventional techniques, the ability to engineer small gap nanoantennas is very important for next generation plasmonic devices, with applications in biochemical sensing, enhanced Raman scattering and plasmonic optical trapping.

4.2 Plasmonic film

Our p-BNA structure has been used to record optical intensity in the near field. We showed direct laser writing of image data or recording the polarization structure of optical vector beams. Using SEM again, we were able to carefully change the radius of curvature of the p-BNAs as a result of plasmonic heating [31] and that permitted us to spatially tune of the resonance. We refer to this as "plasmonic film" similar to the photographic film that was demonstrated by French inventor Nicéphore Niépce in the 19^{th} century [32]. It shows that the localized surface plasmon resonance (LSPR) of the p-BNA can be tuned over 100 nm in the visible spectral region using subtle, photothermally induced morphological changes in the gold bowtie nanoantenna. As the gold on top of the SiO_2 pillars works as localized heat points, the thermal conduction goes down compared to a substrate bound device. Plasmonic film is capable of recording the optical intensity history using continuous wave illumination with very low power ranging from 0 to 2.8

μWm^{-2} as shown in figure 4.5a. Using a continuous wave laser of 660 nm wavelength with a collar adjustable, 0.6 numerical aperture objective (Olympus LUCplanFLN 40X), which produces an approximately Gaussian intensity distribution with an e^{-2} focal radius of ~670 nm, the p-BNAs were heated to change their radius of curvature carefully. We have carefully increased the power from 100 µW to 4 mW, which corresponds to dosages from 0 to 2.8 mW um^{-2}; the color of the exposed region visibly changes as seen in figure 4.5a. After carefully writing small blocks of areas with different power dosages, we take SEM images of those areas, and it can be seen in figure 4.5b. In the SEM, starting from top left to bottom right, the dosage increases, and if we look into the SEMs, we can see a change in the radius of curvature of the bowties. As we increase the dosage, because of the photothermally induced morphological change, the radius of curvature increases and thus takes the shape of a spherical particle due to surface tension [33]. The reflectance spectra have been measured as well on those small blocks of writing by measuring the spectral reflectance

$$R = 1 - [Rraw/\max(Rraw)\,]$$

where Rraw is the raw reflectance obtained by focusing a spatially coherent, supercontinuum source onto the small blocks where the dosage changed from 0 to 2.8 mWµm^{-2}. The experimental and simulated spectra are shown in figure 4.5c and 4.5d respectively. According to figure 4.5c, we can see a clear difference in the reflection spectrum in terms of the dosages.

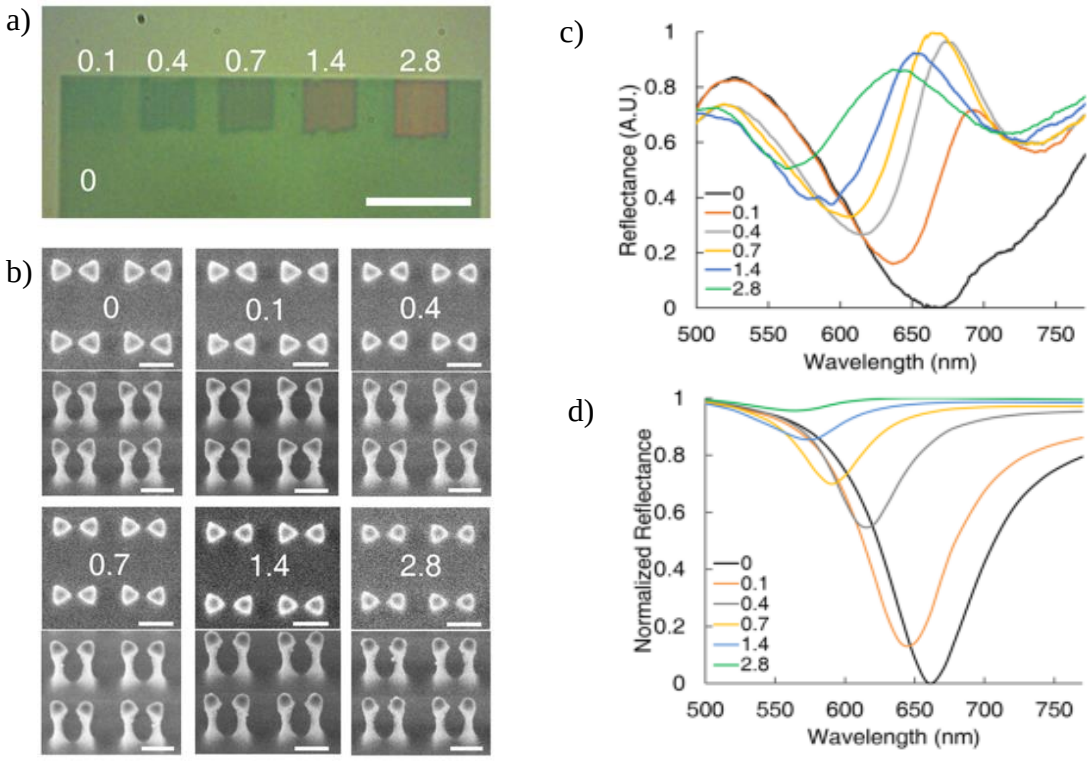

Figure 4.5: a) Optical image of the plasmonic film showing different dosages ranging from 0 to 2.8 mW-μm^{-2}, b) the top and tilted SEM images of the dosage map, c) experimental spectra response of the peak shift as a function of dosage, and d) corresponding theoretical results [26]

It has been convincingly shown that we can record the history of the intensity by the LSPR shift in analogy to the chemical changes in silver halide crystals that form images in standard photographic film. To actually show the demonstration of plasmonic film using our p-BNAs, we have used two ways: 1) using a spatial light modulator (SLM) and 2) using controlled microscope stage movement to write a desired image. As shown in figure 4.6a, the experimental setup for the reflective SLM consists of a conjugate plane of the back aperture of the 0.6 NA exposure lens by means of a beam expanding telescope. An 8 bit, phase only modulator (Boulder Nonlinear Systems, SN7548) SLM was used in this experiment. Using the iterative Gerchberg-Saxton algorithm [34-35], Fourier transforms of the final desired images were generated. Figure 4.6b shows stills from a walking man

movie where the movie frames are recorded subsequently using 660 nm laser source, which forms the final image at the focal plane of the microscope objective. In the second method, we have used controlled movement of the microscope stage to scan a focused Gaussian beam over our p-BNAs. We wrote the letter "I" to show the encoding of information using this technique in our sample. This method can be used to write any kind of channel in our sample for particle manipulation, and by using a laser-scanning galvanometer mirror [36], we can create even longer channels or more elaborate shapes with precision.

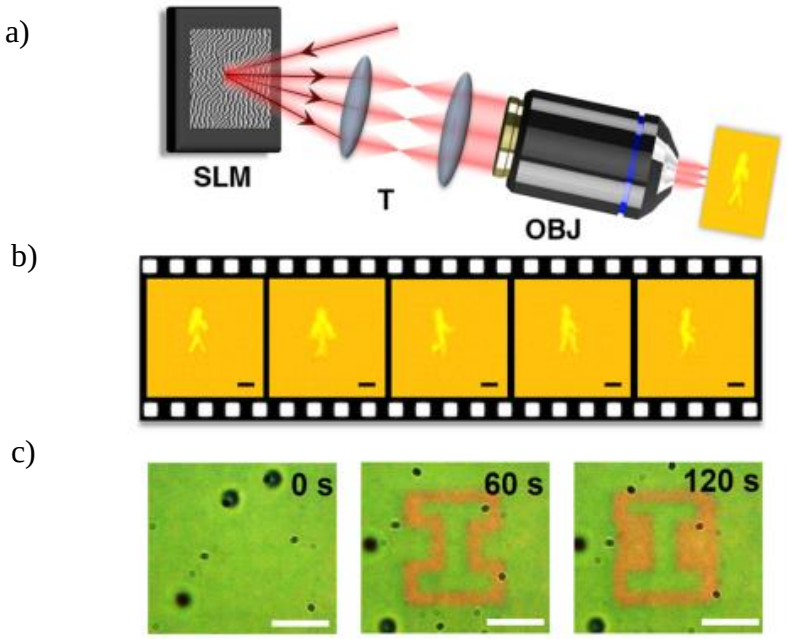

Figure 4.6: a) SLM-based exposure whereby a phase hologram is projected from the SLM, b) each frame of the movie recorded in the plasmonic film, c) scanning stage based exposure whereby the logo "I" has been written in the plasmonic film [26]

4.3 Large bowtie nanoantenna

One of the other studies that we have done is that we doubled the size of the bowtie nanoantennas to operate the nanoantennas in near infrared region with different design parameters. Here, we performed a systematic experimental study exploring the influence of BNA gap spacing, array spacing and pillar height on plasmon resonance wavelength tunability and maximum field enhancement. According to our simulation results the plasmon response can be tuned from 1.3 μm to 2 μm as shown in figure 4.7d and a maximum enhancement of ~8000 is achievable. By comparing figure 4.7c and 4.7d, we can see that our experimental results also match really well with the simulation results. So, we increased the size of the nanoantennas to be 240 nm, shown in figure 4.7a and 4.7b, and thus because of higher charge density and sharper tips, we get better coupling between the nanoantennas and thus the wavelength shifts to near infrared region [37]. Also, because of putting the nanoantennas in the pillars, the effective refractive index n_{eff}, of the overall surrounding medium increases [38]; thus, the sensitivity gets higher and according to the simulation we get the sensitivity to be around 1400 nmRIU-1.

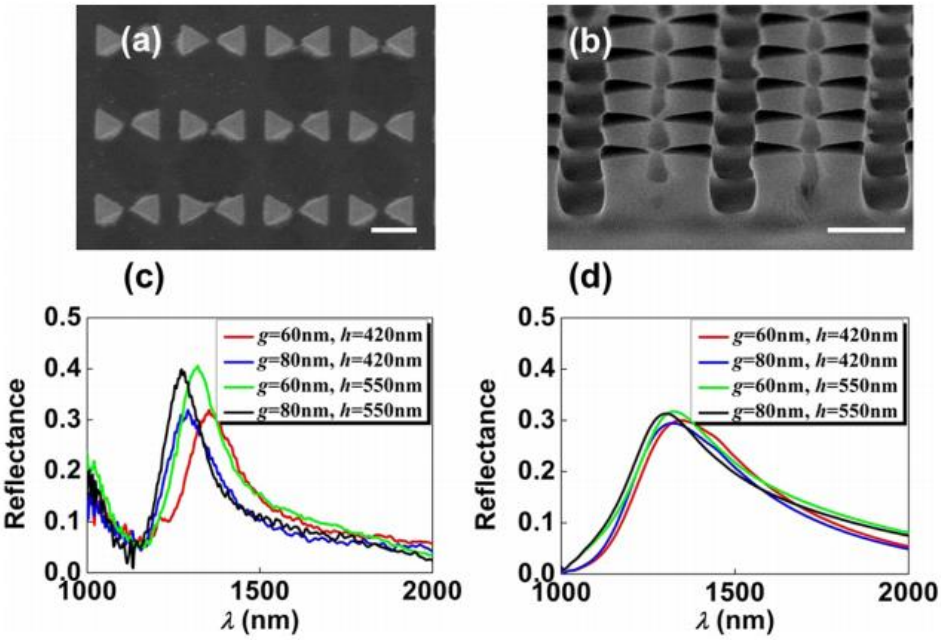

Figure 4.7: a-b) Top and 75^{0} tilted SEM views of the large P-BNA, scale bars are 500 nm, c) experimentally obtained near IR reflection spectra of the P-BNA, and d) corresponding theoretical results [29]

Chapter 5

Future Application and Conclusion

5.1 Future application

After finishing the above mentioned projects, in the near future, we plan to look into changing the refractive index of the surrounding medium by putting the p-BNAs in different solutions. We already started to look into water solution and got some really exciting results. By putting them in water, we can reduce the heating effect of the pillars as water works as a heat sink. In that case, we can use very high power without fear of melting of the gold as we did in the plasmonic film. But now when we increase the power of the fs pulsed laser to be around 100 mW, we can have an effect on the adhesion energy. Putting the sample in water can actually create a lower binding energy between the pillars and the metals. Therefore, having a high power laser in water can break the bond between the metals and the pillars to etch out the metals from the top of the pillars. It can be done within the diffraction limit, but the most interesting thing that we have noticed is that we can shine the laser in a particular area and that area within a chip can have its metal etched out. We call this technique “optical etching” and it is illustrated in figure 5.1a and 5.1b, which show the before and after effect of optical etching. One of the interesting applications that we are looking into at this moment is to fabricate heterogeneous p-BNAs, which is very difficult using conventional electron beam lithography. We do an optical etch and then we deposit any metal, for example, aluminum, and thus create a p-BNA structure which has in one row a combination of 50 nm gold and 50 nm aluminum and the optically etched part has just 50 nm aluminum as shown in figure 5.1c. It can potentially give us very interesting results that we are planning to explore in the near future. So, from this example, we can see that we have many exciting future applications coming up for this p-BNA structure.

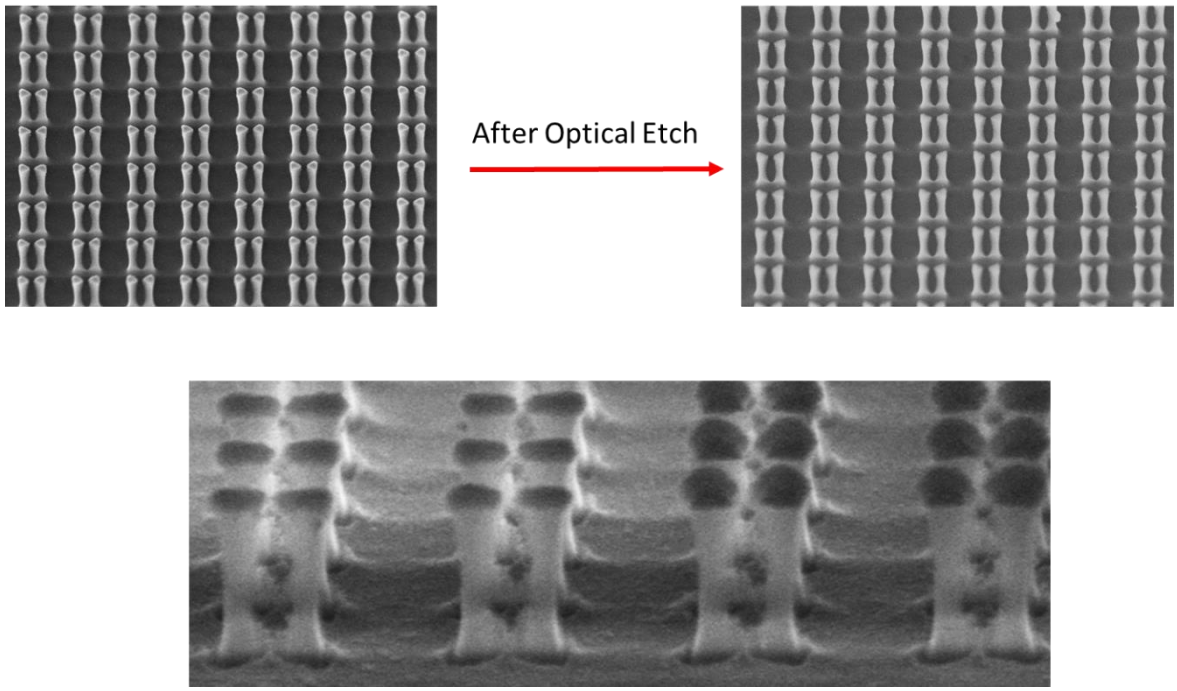

Figure 5.1: a) P-BNA array, b) P-BNA arrays after optical etch, c) Heterogeneous metal stack of aluminum and gold. Scale bar 500 nm for figure a and b, 250 nm for figure c.

5.2 Conclusion

In this thesis, we have shown that fabricating p-BNAs has opened up a new avenue of research in the field of plasmonics. We have given a brief background on light-matter (especially metal) interaction and the theory behind high electric field enhancement. We discussed the different fabrication techniques, specifically lithography, etching and evaporation, that are needed to fabricate the structure in terms of theory. We found out that we needed electron beam lithography as high resolution for our structure was needed because of the 20-40 nm gap between our optical antennas to create high electric field enhancement. We also looked into electron beam evaporation to understand thin film growth. We have also described the steps for the nucleation and growth process of thin

films. We looked into etching techniques, especially dry etching techniques, to understand the etching mechanism. We also explained the reason for choosing RIE to etch SiO_2 pillars. Understanding the theory also made it possible for us to choose different parameters of the respective machines precisely. Then we explained the reasons behind choosing parameters for different techniques to build up the recipe. We also added nickel on top to use that as a protective layer in the case of dry etching. We explained the reasons for creating plasmon induced gradient force to reduce the gap between the nanoantennas. We experimentally showed that we can control accelerating voltage, current and magnification to reduce the gap between nanoantennas to be as low as ~5 nm. We have seen that it enhances the electric field and it is a good candidate for future sensing applications. Lastly, we have looked into the future applications that can be brought forth by the p-BNA structure. Overall, we are looking at an exciting future for the field of plasmonics because of the new avenue of research that has been explored and will continue to be explored via the p-BNA structure.

References

1. Stutzman, W.L., and G.A. Thiele. *Antenna theory and design*. John Wiley & Sons, 2012.

2. Schuller, J.A., E.S. Barnard, W. Cai, Y.C. Jun, J.S. White, and M.L. Brongersma. "Plasmonics for extreme light concentration and manipulation." *Nature materials* 9, no. 3 (2010): 193-204.

3. Mayer, K.M., and J.H. Hafner. "Localized surface plasmon resonance sensors." *Chemical reviews* 111, no. 6 (2011): 3828-3857.

4. Jackson, J.D. *Classical electrodynamics*. Vol. 3. New York: Wiley, 1962.

5. Willets, K.A., and R.P.V. Duyne. "Localized surface plasmon resonance spectroscopy and sensing." *Annu. Rev. Phys. Chem.* 58 (2007): 267-297.

6. Prodan, E., C. R., N.J. Halas, and P. Nordlander. "A hybridization model for the plasmon response of complex nanostructures." *Science* 302, no. 5644 (2003): 419-422.

7. Nie, S., and S. R. Emory. "Probing single molecules and single nanoparticles by surface-enhanced Raman scattering." *Science* 275, no. 5303 (1997): 1102-1106.

8. Grigorenko, A. N., N. W. Roberts, M. R. Dickinson, and Y. Zhang. "Nanometric optical tweezers based on nanostructured substrates." *Nature Photonics* 2, no. 6 (2008): 365-370.

9. Kim, S., J. Jin, Y-J. Kim, I-Y. Park, Y. Kim, and S- W Kim."High-harmonic generation by resonant plasmon field enhancement." *Nature* 453, no. 7196 (2008): 757-760.

10. Zhang, H., M. Zhao, and L. Peng. "Nonlinear structured illumination microscopy by surface plasmon enhanced stimulated emission depletion."*Optics express* 19, no. 24 (2011): 24783-24794.

11. Liao, L., Q. Zhang, Z. Su, Z. Zhao, Y. Wang, Y. Li, X. Lu et al. "Efficient solar water-splitting using a nanocrystalline CoO photocatalyst." *Nature nanotechnology* 9, no. 1 (2014): 69-73.

12. Madou, M. J. *Fundamentals of microfabrication: the science of miniaturization*. CRC Press, 2002.

13. Powell, R. A., ed. *Dry etching for microelectronics*. Elsevier, 2012.

14. Krall, N. A., A. W. Trivelpiece, and R.A. Gross. "Principles of plasma physics." *American Journal of Physics* 41, no. 12 (1973): 1380-1381.

15. Kern, W. *Thin film processes II*. Vol. 2. Academic Press, 2012.

16. Hayat, M.A. *Principles and techniques of scanning electron microscopy. Biological applications. Volume 1*. Van Nostrand Reinhold Company, 1974.

17. Unakar, N. J., J. Y. Tsui, and C. V. Harding. "Scanning electron microscopy."*Ophthalmic Research* 13, no. 1 (1981): 20-35.

18. Roxworthy, B. J., A. M. Bhuiya, X. Yu, E.K.C Chow, and K.C. Toussaint Jr. "Reconfigurable nanoantennas using electron-beam manipulation." *Nature communications* 5 (2014).

19. De Broglie, L. "The reinterpretation of wave mechanics." *Foundations of Physics* 1, no. 1 (1970): 5-15.

20. Pease, R. F. W. "Electron beam lithography." *Contemporary Physics* 22, no. 3 (1981): 265-290.

21. Didier, F., and J. Jupille. "The van der Waals contribution to the adhesion energy at metal-oxide interfaces." *Surface science* 314, no. 3 (1994): 378-384.

22. Heller, J. "Reactive sputtering of metals in oxidizing atmospheres." *Thin Solid Films* 17, no. 2 (1973): 163-176.

23. Bonakdar, A., J. Kohoutek, D. Dey, and H. Mohseni. "Optomechanical nanoantenna." *Optics letters* 37, no. 15 (2012): 3258-3260.

24. Zheng, K., C. Wang, Y-Q. Cheng, Y. Yue, X. Han, Z. Zhang, Z. Shan et al. "Electron-beam-assisted superplastic shaping of nanoscale amorphous silica." *Nature communications* 1 (2010): 24.

25. De A., F.J. García. "Momentum transfer to small particles by passing electron beams." *Physical Review B* 70, no. 11 (2004): 115422.

26. De A., F.J. García. "Optical excitations in electron microscopy." *Reviews of modern physics* 82, no. 1 (2010): 209.

27. Batson, P. E., A. R-Coronado, R. G. Barrera, A. Rivacoba, P. M. Echenique, and J. Aizpurua. "Nanoparticle movement: Plasmonic forces and physical constraints." *Ultramicroscopy* 123 (2012): 50-58.

28. Zheng, H. "Using molecular tweezers to move and image nanoparticles."*Nanoscale* 5, no. 10 (2013): 4070-4078.

29. Reyes-Coronado, A., Rubén G. B., P. E. Batson, P. M. Echenique, A. Rivacoba, and J. Aizpurua. "Electromagnetic forces on plasmonic nanoparticles induced by fast electron beams." *Physical Review B*82, no. 23 (2010): 235429.

30. Tennant, D. M. "Progress and issues in e-beam and other top down nanolithography." *Journal of Vacuum Science & Technology A* 31, no. 5 (2013): 050813.

31. Roxworthy, B. J., A. M. Bhuiya, S. P. Vanka, and K. C. Toussaint Jr. "Understanding and controlling plasmon-induced convection." *Nature communications* 5 (2014).

32. Garrett, A. E. *The Advance of Photography*. Kegan Paul, London, 1911.

33. Kofman, R., P. Cheyssac, A. Aouaj, Y. Lereah, G. Deutscher, T. Ben-David, J. M. Penisson, and A. Bourret. "Surface melting enhanced by curvature effects."*Surface science* 303, no. 1 (1994): 231-246.

34. Goodman, J. W. "Introduction to Fourier Optic." Mac. Graw-Hill, New York (1960).

35. Saxton, W. O. "A new computer language for electron image processing."*Computer Graphics and Image Processing* 3, no. 3 (1974): 266-276.

36. Roxworthy, B. J., K. D. Ko, A. Kumar, K. H. Fung, E. K.C. Chow, G. L. Liu, N. X. Fang, and K. C. Toussaint Jr. "Application of plasmonic bowtie nanoantenna arrays for optical trapping, stacking, and sorting." *Nano letters* 12, no. 2 (2012): 796-801.

37. Halas, N. J., S. Lal, W-S. Chang, S. Link, and P. Nordlander. "Plasmons in strongly coupled metallic nanostructures." *Chemical reviews* 111, no. 6 (2011): 3913-3961.

38. Anker, J. N., W. P. Hall, O. L., N. C. Shah, J. Zhao, and R. P. V. Duyne. "Biosensing with plasmonic nanosensors." *Nature materials* 7, no. 6 (2008): 442-453.